ChemComm

COMMUNICATION

View Article Online
View Journal | View Issue

Cite this: *Chem. Commun.*, 2025, **61**, 1621

Received 28th October 2024,
Accepted 12th December 2024

DOI: 10.1039/d4cc05742b

rsc.li/chemcomm

N skeleton-regulated cobalt phthalocyanine promotes polysulfide adsorption and redox kinetics†

Jiaqi Zhao,[a] Zhanwei Xu,*[a] Yujiao Zhang,[b] Kai Yao,[c] Liang Li,[a] Hang Niu,[a] Jiayin Li [a] and Zhi Li *[d]

An N skeleton substituent on cobalt phthalocyanine (CoPc) was meticulously studied to redistribute the charge in phthalocyanine, improve the mass diffusion, and promote the redox kinetics of polysulfides (LiPS), resulting in a significant ultra-low capacity decay of 0.11% at 5C over 500 cycles.

Lithium–sulfur batteries are regarded as the most promising energy storage systems due to their high theoretical capacity.[1,2] However, the commercialization of lithium–sulfur batteries is hindered by the shuttle effect and sluggish redox kinetics of the intermediate polysulfides (LiPS), causing a severe capacity decay.[3–9] Therefore, many strategies have been devoted to alleviating these issues, such as cathode design,[10–12] electrolyte additives[13,14] and separator modification.[15,16] Separator modification with polar materials is regarded as one of the most effective strategies to inhibit LiPS shuttling directly.

Metal phthalocyanines (MPc) are well known for their macro ring conjugated structure and M–N_4 catalytic center, accomplishing excellent electron transfer efficiency during redox reaction.[17,18] Derivations of MPc with various substituent groups have been reported in the past few years, like –F,[19] –Cl,[20] –NH_2,[21] –NO_2,[22] –SO_3H,[23] –SO_3[24] and so on. However, the introduced electron-rich groups increase the steric hindrance in capturing LiPS and slow down the mass transfer. In contrast, the skeleton substituent may regulate the macro ring conjugated effect and, therefore, the catalytic activities without introducing additional steric hindrance.

Herein, CoTAP and CoPTpz were synthesized on reduced graphene oxide (rGO) by introducing N atoms into the skeleton of the CoPc molecule. Pyridine N atoms exhibit excellent adsorption capability towards LiPS. When introduced into phthalocyanine, N substituent atoms promote the overall conjugation effect in phthalocyanine molecules, regulate the surface charge distribution, promote electron transfer, and strengthen the LiPS inhibiting ability. The electron density difference analysis proves that the introduced pyridine N atoms strengthen the Li–N binding, which causes weakened terminal Li–S binding in LiPS and promotes reduced conversion kinetics. The mass migration rate of Li^+ and LiPS are improved, indicating a decrement of electrochemical polarization. The enhanced mass migration rate alters the Li_2S precipitation morphology from 2D-sheet-like to a porous Li_2S interlayer structure with reduced ion diffusion distance. The resulting cell with CoPTpz/rGO exhibits excellent electrochemical performance with outstanding cycling stability and a low-capacity decay of 0.78% at 5C after 500 cycles.

The CoPc molecule can be divided into two moieties: the inner macrocycle around Co with alternating C and N atoms, and isoindole ligands, as shown in Fig. 1a. The atoms in CoPc are marked according to the distance to the central Co atom. When introducing N atoms on C_3 sites of each isoindole moiety, CoTAP is obtained. CoPTpz is obtained by substituting all C3 and C3′ sites with N atoms. To understand the surface charge distribution in CoPc, CoTAP, and CoPTpz molecules, the surface electrostatic potential maps are shown in Fig. 1b, where red regions represent positive electrostatic potential, and the blue regions indicate negative electrostatic potential (detailed in Fig. S1, ESI†). Compared to the CoPc molecule, the Co centers of CoTAP and CoPTpz appear notably more intensive red, indicating a higher electrostatic potential, which can be ascribed to the charge regulation after introducing the skeleton N atoms. The negative potential concentrated on the N

[a] *Shaanxi Key Laboratory of Green Preparation and Functionalization for Inorganic Materials, Shaanxi University of Science and Technology, P. R. China. E-mail: xuzhanwei@sust.edu.cn*
[b] *Ramu NiCo Management (MCC) Limited Shuguangxili, Chaoyang District, Beijing 100028, P. R. China*
[c] *Forschungszentrum Jülich GmbH, Institute of Energy Materials and Devices (IMD) IMD-2: Materials Synthesis and Processing Wilhelm-Johnen-Str., 52425 Jülich, Germany*
[d] *Department of Chemical and Materials Engineering, University of Alberta, Edmonton Alberta T6G 2 M9, Canada. E-mail: zhi.li@ualberta.ca*

† Electronic supplementary information (ESI) available. See DOI: https://doi.org/10.1039/d4cc05742b

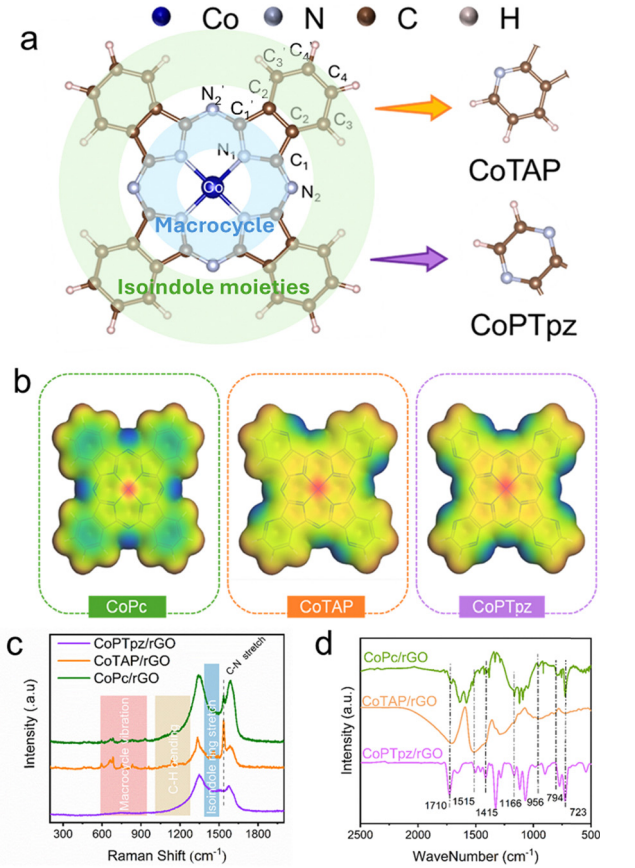

Fig. 1 (a) The atomic structures of CoPc, CoTAP, and CoPTpz. (b) The corresponding surface electrostatics. (c) The Raman spectra of CoPc/rGO, CoTAP/rGO and CoPTpz/rGO. (d) The FTIR spectra of CoPc/rGO, CoTAP/rGO and CoPTpz/rGO.

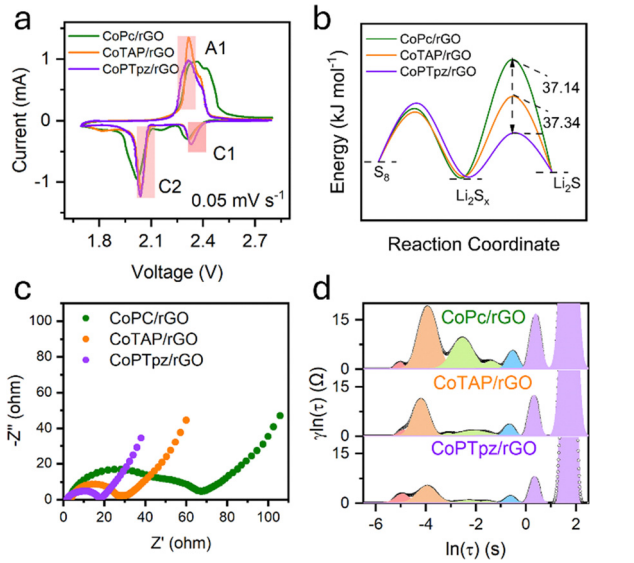

Fig. 2 (a) CV curves of CoPc/rGO, CoTAP/rGO and CoPTpz/rGO. (b) The calculated relative activation energy. (c) EIS spectra after 100 cycles. (d) The corresponding DRT curves.

skeleton atom promotes the adsorption of LiPS and may reduce the coordination effect between the macrocyclic ligand and Co.

The Raman spectra are shown in Fig. S2 (ESI†) and Fig. 1c. The detailed Raman shifts of CoPc, CoTAP, and CoPTpz are displayed in Table S1 (ESI†). The Co–N stretches of CoPc, CoTAP, and CoPTpz are located at 198.5 cm^{-1}, 195.2 cm^{-1}, and 192.5 cm^{-1}. The displacement towards the lower region demonstrates the weakening of Co–N binding, proving the result of surface electrostatic potential. The Raman peaks from 600 cm^{-1} to 900 cm^{-1} are all attributed to the macrocycle vibration, indicating the successful formation of phthalocyanine compounds. The FTIR spectra are displayed in Fig. 1d. The CoPc/rGO, CoTAP/rGO, and CoPTpz/rGO exhibit the same characteristic peaks. The peaks around 723 cm^{-1} and 794 cm^{-1} correspond to the C–C out-of-plane ring deformation and C–N in-plane stretching vibration of the phthalocyanine ring, respectively. The peak around 856 cm^{-1} is attributed to the Co ligand vibration in the center of the phthalocyanine. The peaks around 1535 cm^{-1} and 1627 cm^{-1} correspond to the C=N stretching and C=C macrocycle deformation.

The XPS spectra of Co 2p and N 1s are shown in Fig. S3 (ESI†). The Co–N binding of CoPc/rGO is located at 781.2 eV and 796.7 eV. After introducing the skeleton N atoms, the Co–N peaks are all shifted to the higher region, indicating that the electron density of the Co–N bond is weakened. The morphologies of CoPc/rGO, CoTAP/rGO and CoPTpz/rGO are shown in Fig. S4 (ESI†). The amorphous CoPc, CoTAP and CoPTpz all tile on the rGO surface with nanorods or nanoparticles around 200 nm. The pore size distributions are measured by the BET test (Fig. S5, ESI†). The CoPc/rGO and CoPTpz/rGO show similar pore structures at 1.8 nm and around 40.0 nm, while the CoTAP/rGO exhibits a higher pore volume at 1.8 nm and a smaller mesopore width at around 19.8 nm, which may promote the redox kinetics. The penetration tests are measured by H-type electrolytic cells. After 24 h standing, the CoPTpz/rGO separator shows lighter color as well as lower concentration of penetrated Li_2S_6, which is proved by the following UV-vis spectra (Fig. S6, ESI†).

To evaluate the redox kinetics of various skeleton substituent CoPc, CV curves measured at 0.05 mV s^{-1} are displayed in Fig. 2a. In peak C1, the irreversible reduction potentials of CoPc/rGO, CoTAP/rGO and CoPTpz/rGO are 2.31 V, 2.32 V and 2.33 V, respectively. The positively shifted potential demonstrates the promoted reduction kinetics of solid–liquid conversion. Peaks C2 and A1 could be attributed to the conversion between LiPS and Li_2S_2/Li_2S. The CoTAP/rGO and CoPTpz/rGO show similar reduction potentials around 2.04 V and 2.31 V, which is promoted compared to CoPc/rGO of 2.02 V and 2.33 V. These results are consistent with the BET results and demonstrate that the skeleton N substituent could improve the conversion kinetics for all sulfur species. Fig. S7g (ESI†) displays the Li^+ diffusion coefficient (D_{Li^+}) in various conversion processes, calculated based on the Randles–Sevcik (eqn (S1), ESI†) of the CV curves from 0.01 to 0.05 mV s^{-1} (Fig. S7a–f, ESI†). The introduced skeleton N atoms could enhance the Li^+ diffusion rate around the three main redox peaks. For example, the D_{Li^+} of CoTAP/rGO and CoPTpz/rGO at peak C1 increases from 7.95 × 10^{-12} cm^{-2} s^{-1} to 9.31 × 10^{-12} cm^{-2} s^{-1} and

1.42×10^{-11} cm^{-2} s^{-1}. Also, the corresponding Tafel slopes of the three main redox peaks are displayed in Fig. S7h and i (ESI†). The CoPTpz/rGO exhibits the lowest Tafel slope of all three peaks, indicating the enhanced redox dynamics. To gain further insight into the effect of skeleton N towards LiPS conversion, the relative activation energy (E_a) was calculated according to eqn (S2) (ESI†). In the reduction process of S_8 towards Li_2S_x, the E_{a1} value of the CoPc/rGO, CoTAP/rGO and CoPTpz/rGO samples shows a similar value. Compared to the CoPc/rGO, the E_{a2} values of CoTAP/rGO and CoPTpz/rGO between Li_2S_x and Li_2S are decreased by 37.14 kJ mol^{-1} and 74.48 kJ mol^{-1}, demonstrating the reduction of the conversion activation energy.

The Tafel plots of S||S symmetric cells with three samples are depicted in Fig. S8 (ESI†). The cell with the CoPTpz/rGO interlayer exhibits a higher exchange current of 0.0273 mA than CoTAP/rGO of 0.0230 mA, and CoPc/rGO of 0.0144 mA, demonstrating the improvement of the intrinsic electron transfer kinetics and interfacial reaction kinetics by the introduced N substituents. All of the above results demonstrate that skeleton N atoms could accelerate both the Li^+ diffusion rate and LiPS conversion kinetics.

Galvanostatic intermittent titration technique (GITT) curves display that the CoPTpz/rGO exhibits the lowest ΔIR value in all charge/discharge processes, especially in Li_2S activation and nucleation regions (Fig. S9a–d, ESI†), indicating the smallest Ohm resistance. The EIS spectra of CoPc/rGO, CoTAP/rGO, and CoPTpz/rGO after 100 cycles are displayed in Fig. 2c. The CoPTpz/rGO exhibits the lowest charge transfer resistance. To further investigate the overlapping electrochemical resistance, distribution of relaxation times analysis (DRT) was used (Fig. 2d). The resistances of various peaks are decreased by introducing more pyridine N substituents. Those peaks located at −0.6 s, 0.3 s, and 1.7 s are attributed to the diffusion of LiPS and the diffusion of Li^+ (Fig. S10, ESI†), indicating the improvement of the diffusion procedure.

The liquid–solid conversion performance of the CoPc/rGO, CoTAP/rGO, and CoPTpz/rGO catalysts is displayed in Fig. S11a–c (ESI†). The CoPTpz/rGO exhibits the highest precipitation capacity of 731.3 mA h g^{-1}, indicating the promoted shuttle-inhibiting effect of LiPS. The corresponding current–time transient curves were used to investigate the precipitation behaviors of the CoPc/rGO, CoTAP/rGO, and CoPTpz/rGO catalysts (Fig. S11d–f, ESI†). The theoretic deposition model can be divided into lattice incorporation growth (2DI and 2DP) and bulk diffusion-controlled growth (3DI and 3DP) with a 2D-plate-like morphology and 3D-sphere-like morphology, respectively. The deposition model of CoPc/rGO could be attributed to the 3DI and 2DI hybrid model, which is proved by the SEM image (Fig. S11g–i, ESI†). With the pyridine N atoms introduced, the 2D-plate like Li_2S decreases obviously.

To further evaluate the adsorption capability of CoPc and its skeleton substituents towards LiPS, density functional theory (DFT) calculations were employed. The optimal adsorption configurations with the corresponding adsorption energies between sulfur species and CoPc, CoTAP, and CoPTpz are shown in Fig. S12 (ESI†) and Fig. 3a. The adsorption energies towards soluble Li_2S_6 and solid Li_2S_2/Li_2S are all increased by introducing more skeleton N atoms. The adsorption energies for the S_8 molecule show a decrement along with an increase of the N atom, indicating that the N substituents on the CoPc backbone are oleophobic due to the concentrated charge. Enhanced adsorption energy could strongly promote the efficiency of anchoring LiPS, further inhibiting the shuttling of LiPS.

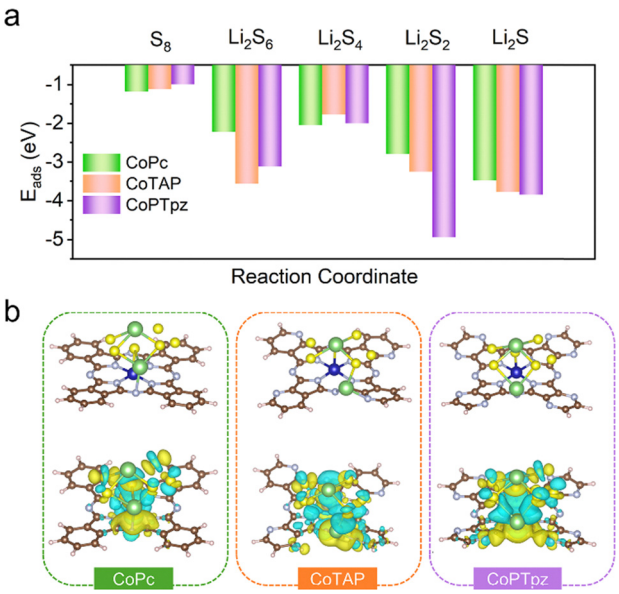

Fig. 3 (a) The adsorption energies of all optimized structures. (b) The electron density differences of CoPc, CoTAP and CoPTpz with Li_2S_6. The blue and yellow regions indicate the accumulation of positive and negative charges, respectively.

Detailed charge density difference analysis of Li_2S_6 on CoPc, CoTAP, and CoPTpz is shown in Fig. 3b. The interaction between Li_2S_6 and phthalocyanine could be visualized *via* the electron density region. In all three phthalocyanine molecules, the central Co–N_4 site exhibits strong electron accumulation, indicating that Co–S binding is formed. The introduced N atoms on the molecular skeleton enable a promoted affinity toward Li from LiPS by forming Li–N binding. The CoPTpz exhibits the most stable adsorption configuration and the weakest Li–S binding in captured LiPS, which is proved by electron accumulation and loss, respectively. The improved cutting-off ability towards Li–S binding also implies the reduction of conversion active energy.

The rate performances of various catalysts are illustrated in Fig. 4a and Fig S13a (ESI†). Rate capacity is promoted by introducing the skeleton N atoms. CoPTpz/rGO exhibits an ultrahigh initial capacity at 0.2C to 2C. Along with the increase of current density, the discharge capacity of CoPTpz/rGO becomes much more similar to CoTAP/rGO at 4C, indicating the limited performance promotion effect of N skeleton atoms. The corresponding charge–discharge curves of the CoPc/rGO, CoTAP/rGO, and CoPTpz/rGO catalysts are displayed in Fig. S13b–d (ESI†).

The charge–discharge curves of cells with various catalysts in the cycle at 0.2C are displayed in Fig. 4b. The CoPTpz/rGO

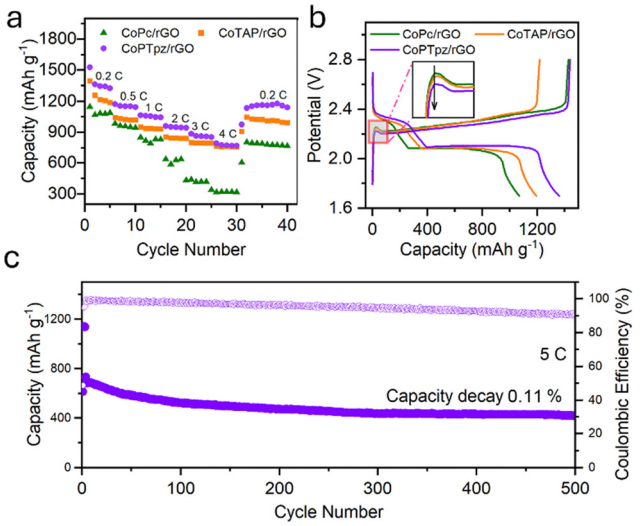

Fig. 4 (a) Rate performance of CoPc/rGO, CoTAP/rGO, and CoPTpz/rGO. (b) The charge–discharge curves at 0.2C of various catalysts. (c) Long-term cycling performance of CoPTpz/rGO at 5C for 500 cycles.

exhibits the highest discharge plateaus and capacity. The charge curve could be associated with the Li_2S activation energy. The Li_2S activation barriers of CoPc/rGO, CoTAP/rGO, and CoPTpz/rGO are 2.26 V, 2.25 V, and 2.23 V, respectively. This result demonstrates that the skeleton N atoms could decrease the LiPS conversion energy. The cycling performance of CoPTpz/rGO with a sulfur loading of 2.75 mg cm^{-2} at 0.2C is shown in Fig. S13e (ESI†). The discharge capacity increases at the initial several cycles, which could be attributed to the active procedure. After 350 cycles, CoPTpz/rGO could still retain 636.2 mA h g^{-1}. The long-term cycling performance of the CoPTpz/rGO catalysts is shown in Fig. 4c. The CoPTpz/rGO catalyst exhibits an initial capacity of 681.3 mA h g^{-1} at 5C, and after 500 cycles, the capacity remains 413.2 mA h g^{-1} with a low-capacity decay of 0.11% per cycle. The ultra-stable cycling performance demonstrates the promoted redox reversibility and shuttling inhibition. Although it is difficult to compare the performance of Li–S batteries in the literature given the variation in testing conditions, the long-term cyclingperformance of CoPTpz/rGO is outstanding among similar catalysts containing Co–N_4 sites that are usually measured under lower current density (Table S2, ESI†).[25–29]

In summary, the redox kinetics and electrochemical performance of CoPc derivatives are significantly improved by introducing more pyridine N in the skeleton, serving as extra lithophilic sites for LiPS adsorption *via* stronger Li–N binding. The pyridine N substituent on the CoPc skeleton regulates the charge distribution and promotes the mass transfer rate in electrolytes. Improved both Li^+ and LiPS diffusion rates led to a change of Li_2S precipitation morphology from the 2D/3D hybrid model to the 3D model, implying a faster oxidation procedure of Li_2S. The cell with CoPTpz/rGO exhibits outstanding cycling stability, S reversibility even at 5C, and a low capacity-decay rate of 0.11% after 500 cycles. At the end of this communication, we would like to emphasize that the N skeleton substituent wouldn't change the planar structure of CoPc, and therefore wouldn't weaken the π–π interaction that holds CoPc on the rGO surface. In fact, the lone-pair electrons from the additional N could further strengthen the π–π interaction and make the catalytic site physically more stable. This highlights another advantage of skeleton substituents over other electron regulation strategies that require out of plane modification.

Data availability

All data included in this study are available upon request by contact with the corresponding author.

Conflicts of interest

There are no conflicts to declare.

Notes and references

1 Q. Liang, S. Wang and X. Lu, *et al.*, *ACS Nano*, 2024, **18**(3), 2395–2408.
2 R. Yang, Y. Zhang and X. Chen, *et al.*, *Chem. Commun.*, 2024, **60**(68), 9078–9081.
3 Q. Liang, S. Wang and Y. Yao, *et al.*, *Adv. Funct. Mater.*, 2023, **33**(32), 2300825.
4 Z. Zhao, Y. Pan and S. Yi, *et al.*, *Adv. Mater.*, 2024, **36**(13), e2310052.
5 T. Ren, X. Wang and N. Wang, *et al.*, *J. Mater. Chem. A*, 2024, **12**(9), 5307–5318.
6 J. Yu, C. Huang and O. Usoltsev, *et al.*, *ACS Nano*, 2024, **18**(29), 19268–19282.
7 J. Wang, X. Fan and X. Han, *et al.*, *Adv. Mater.*, 2024, **36**(28), e2312374.
8 Z. Xu, J. Zhao and R. Lin, *et al.*, *J. Power Sources*, 2024, **618**, 235162.
9 L. Ren, K. Sun and Y. Wang, *et al.*, *Adv. Mater.*, 2024, **36**(14), e2310547.
10 Z. Xu, H. Niu and Y. Zhang, *et al.*, *ACS Appl. Nano Mater.*, 2024, **7**(18), 22052–22060.
11 F. Liang, Q. Deng and S. Ning, *et al.*, *Adv. Sci.*, 2024, **11**(32), 2403391.
12 C.-C. Wu, Y.-C. Ho and S.-H. Chung, *J. Mater. Chem. A*, 2023, **11**(45), 24651–24660.
13 Q. Yang, S. Shen and Z. Han, *et al.*, *Adv. Mater.*, 2024, **36**(36), e2405790.
14 L. Liu, Z. Song and Z. Qi, *et al.*, *Chem. Commun.*, 2024, **60**(78), 10910–10913.
15 X. Dong, X. Liu and P. K. Shen, *et al.*, *Adv. Funct. Mater.*, 2023, **33**(3), 2210987.
16 W. Zhao, K. Zhang and F. Wu, *et al.*, *Chem. Eng. J.*, 2023, **453**, 139348.
17 A. B. Sorokin, *Chem. Rev.*, 2013, **113**(10), 8152–8191.
18 H.-g Wang, Q. Wu and L. Cheng, *et al.*, *Energy Storage Mater.*, 2022, **52**, 495–513.
19 J. Kim, H. Shin and D. J. Yoo, *et al.*, *Adv. Funct. Mater.*, 2021, **31**, 51.
20 Z. Shi, K. Zhang and K. Xiao, *et al.*, *ACS Appl. Energy Mater.*, 2021, **4**(8), 7743–7750.
21 X. Li, X. Zhao and J. Wang, *et al.*, *Carbon*, 2023, **201**, 307–317.
22 X. Zhao, Y. Zhang and W. Liu, *et al.*, *Adv. Funct. Mater.*, 2023, **34**(13), 2313107.
23 J. Zheng, F. Chen and J. Ding, *et al.*, *Colloids Surf., A*, 2024, **702**, 135074.
24 Z. Chen, K. Gan and Y. Peng, *et al.*, *ACS Appl. Mater. Interfaces*, 2023, **15**(48), 55703–55712.
25 X. Zhao, Y. Zhang and W. Liu, *et al.*, *Adv. Funct. Mater.*, 2024, **34**(13), 2313107.
26 R. Wang, R. Wu and C. Ding, *et al.*, *Nano-Micro Lett.*, 2021, **13**(1), 151.
27 Y. Li, Z. Chen and X.-Y. Zhong, *et al.*, *Adv. Funct. Mater.*, 2024, 2412279.
28 Q. Lv, Y. Sun and B. Li, *et al.*, *Adv. Energy Mater.*, 2024, 2403223.
29 X. Zhao, Y. Xu and T. Qiu, *et al.*, *Energy Storage Mater.*, 2024, **72**, 103728.

